Journal of Geophysical Research: Oceans

RESEARCH ARTICLE
10.1029/2018JC013814

Variability and Redistribution of Heat in the Atlantic Water Boundary Current North of Svalbard

A. H. H. Renner[1], A. Sundfjord[2], M. A. Janout[3], R. B. Ingvaldsen[4], A. Beszczynska-Möller[5], R. S. Pickart[6], and M. D. Pérez-Hernández[6,7]

[1]Institute of Marine Research, Tromsø, Norway, [2]Norwegian Polar Institute, Fram Centre, Tromsø, Norway, [3]Alfred Wegener Institute, Helmholtz Centre for Polar and Marine Research, Bremerhaven, Germany, [4]Institute of Marine Research, Bergen, Norway, [5]Institute of Oceanology, Polish Academy of Sciences, Sopot, Poland, [6]Woods Hole Oceanographic Institution, Woods Hole, MA, USA, [7]Environment Division, Marine and Freshwater Research Institute, Reykjavik, Iceland

Key Points:
- We present year-long records of hydrography and currents of the Atlantic Water boundary current north of Svalbard
- Upper ocean heat loss is 16 W m^{-2} annually with episodic heat loss of >100 W m^{-2} in autumn and winter
- AW inflow drives 80% of heat content variability, with wind-induced mixing and tidal mixing as the other main factors

Supporting Information:
- Supporting Information S1

Correspondence to:
A. H. H. Renner,
angelika.renner@imr.no

Citation:
Renner, A. H. H., Sundfjord, A., Janout, M. A., Ingvaldsen, R., Beszczynska-Möller, A., Pickart, R., & Pérez-Hernández, M., (2018). Variability and redistribution of heat in the Atlantic Water boundary current north of Svalbard. *Journal of Geophysical Research: Oceans*, *123*, 6373–6391. https://doi.org/10.1029/2018JC013814

Received 19 JAN 2018
Accepted 31 JUL 2018
Accepted article online 6 AUG 2018
Published online 12 SEP 2018

Abstract We quantify Atlantic Water heat loss north of Svalbard using year-long hydrographic and current records from three moorings deployed across the Svalbard Branch of the Atlantic Water boundary current in 2012–2013. The boundary current loses annually on average 16 W m^{-2} during the eastward propagation along the upper continental slope. The largest vertical fluxes of >100 W m^{-2} occur episodically in autumn and early winter. Episodes of sea ice imported from the north in November 2012 and February 2013 coincided with large ocean-to-ice heat fluxes, which effectively melted the ice and sustained open water conditions in the middle of the Arctic winter. Between March and early July 2013, a persistent ice cover-modulated air-sea fluxes. Melting sea ice at the start of the winter initiates a cold, up to 100-m-deep halocline separating the ice cover from the warm Atlantic Water. Semidiurnal tides dominate the energy over the upper part of the slope. The vertical tidal structure depends on stratification and varies seasonally, with the potential to contribute to vertical fluxes with shear-driven mixing. Further processes impacting the heat budget include lateral heat loss due to mesoscale eddies, and modest and negligible contributions of Ekman pumping and shelf break upwelling, respectively. The continental slope north of Svalbard is a key example regarding the role of ocean heat for the sea ice cover. Our study underlines the complexity of the ocean's heat budget that is sensitive to the balance between oceanic heat advection, vertical fluxes, air-sea interaction, and the sea ice cover.

Plain Language Summary The Atlantic Water boundary current carries heat into the Arctic Ocean as it flows through Fram Strait and along the continental slope north of Svalbard. Using observations from bottom-mounted instruments, we investigated different processes leading to heat loss from the Atlantic Water layer in the region north of Svalbard. Most of the changes recorded over the course of 1 year from September 2012 to September 2013 at 81.5°N, 31°E are driven by changes further upstream and by air-sea heat exchange. However, significant local heat loss can be caused by mixing due to wind or tides. Seasonal differences are large and predominantly caused by absence or presence of sea ice (autumn/early winter versus spring/early summer), influence of melt water and wind on the stability of the water column, and a seasonally changing light regime.

1. Introduction

The Atlantic Water (AW) inflow through Fram Strait is the largest oceanic heat source to the Arctic Ocean (Aagaard et al., 1987). The West Spitsbergen Current carries the AW northward in Fram Strait until it splits into several branches (Figure 1): The upper-slope part crosses the Yermak Plateau northwest of Svalbard and enters the Arctic Ocean as the Svalbard Branch (Aagaard et al., 1987); the Yermak branch follows the western Yermak Plateau northward before turning east; and a third part recirculates in Fram Strait (Beszczynska-Möller et al., 2012; Rudels et al., 2014). Time series from long-term mooring deployments show that the volume flux in the West Spitsbergen Current core at 79°N is quite stable (Beszczynska-Möller et al., 2012). The fraction of recirculation in Fram Strait, however, varies seasonally (Hattermann et al., 2016), which in turn likely affects the relative distribution of AW in the Yermak and the Svalbard Branches (Schauer et al., 2004). Further complicating the picture, observations and modeling studies indicate that a third branch crossing Yermak Plateau might be established in winter (Gascard et al., 1995; Koenig et al., 2017). It is still unclear whether these branches

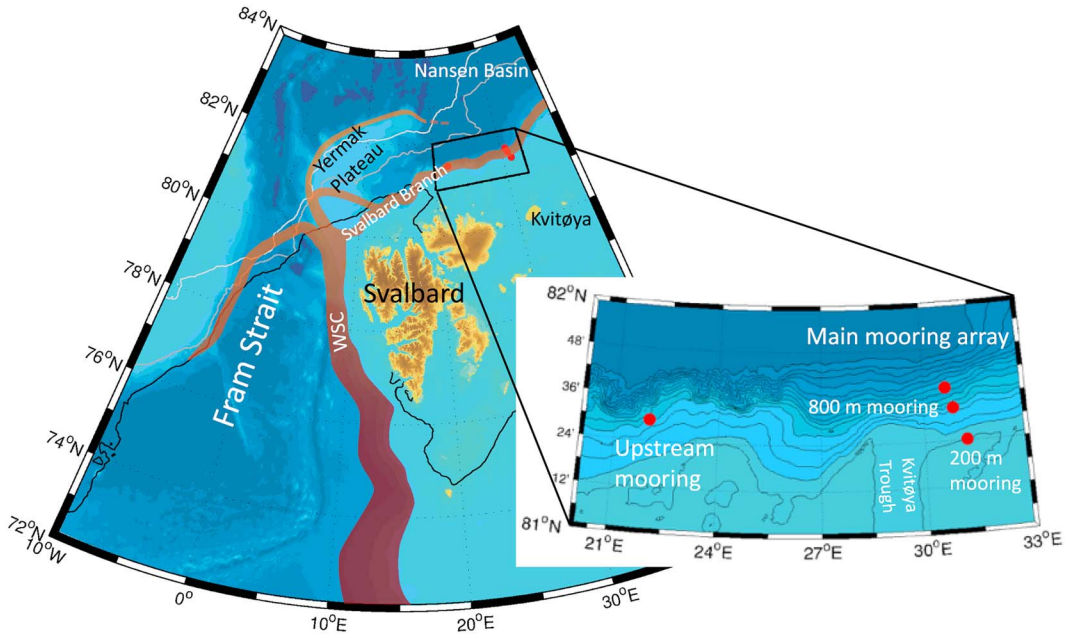

Figure 1. Map of the study region. The red lines on the overview map indicate the pathways of Atlantic Water flowing into the Arctic. The black, dark gray, and light gray lines on the overview map denote the average position of the sea ice edge in March 2013, September 2012, and September 2013, respectively. Red dots in the inset show the positions of the moorings on the outer shelf and upper slope. Bathymetry is taken from IBCAO version 3.0 (Jakobsson, 2012). WSC = West Spitsbergen Current.

merge again east of Yermak Plateau. The continuation of the AW inflow into the Arctic, however, is topographically controlled and predominantly follows the continental slope as part of the Arctic Circumpolar Boundary Current around the perimeter of the deep Arctic Ocean basin (Aagaard, 1989; Aksenov et al., 2011; Rudels et al., 1999).

The slope area north of Svalbard is recognized as an important region for modification of the AW boundary current (Polyakov et al., 2017) and a potential hotspot for tidally driven mixing (Rippeth et al., 2015). However, the northeastern region has been little studied. In a mooring study, Ivanov et al. (2009) document a clear seasonal cycle with warmer and saltier water in autumn than in spring. Ship-based hydrographic transects conducted during summer and autumn show that although the Svalbard Branch is always discernible northeast of Svalbard, it is highly variable in space and time (Cokelet et al., 2008; Pérez-Hernández et al., 2017; Våge et al., 2016). The variability seen in such quasi-synoptic surveys may in part be attributed to frontal instabilities leading to eddy formation. This distorts the mean flow and hydrographic structure and thus adds uncertainty to geostrophic transport calculations (Pérez-Hernández et al., 2017; Våge et al., 2016).

The inflow of warm AW has a major impact on the sea ice cover north of Svalbard. The ice cover in this region is dominated by first- and second-year ice, either locally formed or advected into the area (Renner et al., 2013). However, the AW inflow provides enough heat to keep the area ice free over prolonged periods of time (e.g., Ivanov et al., 2016). This ice-free region has been increasing to the east in recent years (Onarheim et al., 2014; Vinje, 2001), likely as a result of increased oceanic heat transport (Ivanov et al., 2012; Onarheim et al., 2014; Polyakov et al., 2017), which strongly affects a thinning ice cover (Hudson et al., 2013; Koenig et al., 2016; Provost et al., 2017). Observations from the upstream areas over Yermak Plateau and the slope north of Svalbard document large upward heat fluxes above the AW layer of several tens of watts per square meter well below the surface (Meyer et al., 2017) and exceeding 100 W m^{-2} in the under-ice boundary layer during strong wind events (Peterson et al., 2017) or over the steep slope (Koenig et al., 2016). Away from the core of the boundary current, just beyond the continental slope, a late-summer study found boundary layer values ranging from near zero to more than 50 W m^{-2} (mean 13.1 W m^{-2}, Hudson et al., 2013). This is likely in part driven by absorbed solar radiation but nevertheless is substantially higher than measurements from the interior Nansen Basin in winter (2 W m^{-2}, Meyer et al., 2017).

Previous studies have documented how inflowing pulses of warm water from the North Atlantic travel around the Arctic Ocean basin with the boundary current (Polyakov et al., 2005) with significant impact on the Arctic sea ice cover (Polyakov et al., 2010, 2017). Recent measurements from the Eastern Eurasian Basin have shown that the vertical stability of the boundary current may be weakening, allowing more heat to melt the overlying sea ice in that part of the ocean (Polyakov et al., 2017). Mooring data have provided significant insight on the vertical current structure (Pnyushkov et al., 2013), seasonal and interannual variability of the temperature of the AW boundary current (Dmitrenko et al., 2006; Pnyushkov et al., 2015), and the signature of tides over the slope in the Eastern Eurasian Basin (Pnyushkov & Polyakov, 2012). Ship-based campaigns in the same area have documented cross-slope hydrographic properties (Dmitrenko et al., 2011) and vertical mixing rates (Lenn et al., 2009).

In light of the ongoing changes in the Arctic climate system and associated impacts on ecosystems and carbon cycling, improved knowledge about the variability and along-stream modification of the AW in the boundary current north of Svalbard is needed. This paper presents the first full-year multimooring deployment in the Svalbard Branch and focuses on the seasonality of vertical redistribution of heat. The observational data set, processing procedures, and metrics are presented in section 2. Results follow in section 3, with presentations of the overall variability of temperature, currents, and heat content in the upper water column in section 3.1, along-slope heat loss in section 3.2, air-sea heat fluxes and vertical mixing in section 3.3, wind-driven vertical transports in section 3.4, and, briefly, lateral transports in section 3.5. The results are then discussed and summarized in section 4.

2. Methods

2.1. Mooring Data

In September 2012, three moorings were deployed over the outer shelf/upper continental slope north of Kvitøya (81.5°N, 31°E) as part of the Long-term variability and trends in the AW inflow region (A-TWAIN) project (see Figure 1). The moorings were located at the 200-, 500-, and 800-m isobaths and were equipped with temperature and conductivity sensors as well as current meters. Unfortunately, the 500-m mooring was lost, but the other two were recovered successfully in September 2013. For an overview of the sensors deployed and the data return, see Table 1.

The temperature and conductivity measurements were calibrated using shipboard conductivity-temperature-depth (CTD) profiles obtained during the deployment and recovery cruises (Seabird SBE911; see Våge et al., 2016, and Pérez-Hernández et al., 2017, for details regarding processing and calibration and for hydrographic sections taken during the cruises). The SBE37s were found to be in very good agreement with the CTD values at the corresponding depths, and no sensor drift was observed. The SBE16 conductivity values were adjusted to the CTD data collected from the ship. Again, sensor drift was negligible.

Data from the Acoustic Doppler Current Profiler (ADCPs) were filtered for data points with low signal strength, high error velocity, or unrealistically high velocities ($\pm 3 \cdot$ standard deviation). On several occasions, the 800-m mooring was blown down by as much as ~150 m at the uppermost sensor due to strong currents. Magnetic deviation is substantial at high latitudes (around 18° at the main mooring array during this deployment period). Issues with compass calibration prevented using simple rotational adjustment by the deviation applicable during the measurement period. Instead, assuming that the along-shelf current should dominate the current record (e.g., Nøst & Isachsen, 2003), the ADCP and point current meter records were rotated such that the main direction of the observed current follows the direction of the local 200- and 800-m isobaths. To create a combined data set of along- and across-slope currents from the two ADCPs on the 800-m mooring, we derived the currents along the major (along-slope) and minor (across-slope) principle axes of current variance for each ADCP. Using the depth layer between 52 and 76 m where the ADCP measurements overlap, we find that the lower instrument generally overestimates current speeds by almost 30% relative to the upper ADCP. For a conservative approach regarding current and transport estimates, we therefore scaled the lower ADCP to match the upper one and used the values from the upper instrument when both were available. The combined ADCP record of along- and across-slope currents was then detided using a 40-hr, seventh-order Butterworth filter and averaged to obtain daily means.

An additional mooring was located 145 km to the west of the main mooring array (22°E) over the 800-m isobath. The core of the boundary current is typically found over the continental slope between the 700- and 1,000-m isobaths (Ivanov et al., 2009), hence the choice to maintain moorings in this depth interval at two

Table 1
Overview of Instrumentation on the ATWAIN Moorings

Mooring	Instrument	Depth (m)	Record start	Record end
A200	Seabird SBE37	52	Failed	
	Seabird SBE37	104	16 September 2012	15 September 2013
	RDI Workhorse ADCP 150 kHz, upward looking	112	16 September 2012	15 September 2013
	Seabird SBE37	131	16 September 2012	15 September 2013
	Seabird SBE37	180	16 September 2012	15 September 2013
A500	Lost			
A800	Seabird SBE16	25	18 September 2012	16 September 2013
	Seabird SBE16	49	18 September 2012	06 September 2013
	RDI Workhorse ADCP 300 kHz, upward looking	97	18 September 2012	03 September 2013
	Seabird SBE37	101	18 September 2012	16 September 2013
	Seabird SBE37	198	18 September 2012	16 September 2013
	Nortek Continental ADCP 190 kHz, upward looking	244	20 September 2012	16 September 2013
	Nortek Continental ADCP 190 kHz, upward looking	378	Failed	
	Seabird SBE37	399	18 September 2012	16 September 2013
	Aanderaa RCM7	402	18 September 2012	16 September 2013
	Seabird SBE37	751	18 September 2012	16 September 2013
	Aanderaa RCM7	754	18 September 2012	16 September 2013
	Seabird SBE53	851	18 September 2012	17 September 2013
AUPSTREAM	Seabird SBE37	50	28 September 2012	20 September 2013
	Moored McLane Profiler with Seabird SBE52	52–750	28 September 2012	20 September 2013

Note. ADCP = Acoustic Doppler Current Profiler; A-TWAIN = Long-term variability and trends in the Atlantic Water inflow region.

locations along the slope. The upstream mooring contained a McLane Moored Profiler (MMP) with SBE52 sensor recording temperature, conductivity, and pressure and a three-axis acoustic current meter that measured profiles of velocity. The MMP sampled over the depth range 52–750 m, while a Seabird SBE37 MicroCat measuring conductivity, temperature, and depth was located 2 m above the MMP. The MMP obtained profiles at an average interval of 12 hr, while the CTDs recorded every 15 min. The MMP data were interpolated to a regular grid in the vertical (2-m spacing) and merged with the SBE37 data, subsampled in time to match MMP record.

2.2. Environmental Data

Sea surface temperature (SST) was obtained from the Optimum Interpolation Sea Surface Temperature product (OISST v2, available from NOAA/OAR/ESRL PSD, Boulder, Colorado, USA, at https://www.esrl.noaa.gov/psd/; Reynolds et al., 2007; Reynolds, 2009). For sea ice concentration, we used the AMSR-2 derived data set provided by the Institute of Environmental Physics, University of Bremen, Germany (Spreen et al., 2008). Surface wind fields (10 m above sea level), sea level pressure, and surface air temperature (2 m above sea level), as well as air-sea heat and radiative fluxes were extracted from ERA-Interim (Dee et al., 2011). ERA-Interim has a horizontal resolution of 0.75° × 0.75°, which for the study region at 80–82°N corresponds to a much higher resolution in the zonal direction (10.9–14.1 km) as compared to the meridional direction (83.3 km). To obtain values at the mooring locations, data were bilinearly interpolated from the respective nearest grid points onto the moorings positions.

2.3. Heat Content Change Derivation

To assess heat content changes in the upper ocean, we combined SST and temperature observations from the moorings using linear interpolation to fill the gap between the SST record and the uppermost temperature sensor on the moorings. While the resulting interpolated profile will not capture the full variability in the water column, comparison with CTD casts during deployment and recovery shows that moored and shipboard CTD profiles are comparable without systematic bias. Reynolds et al. (2007) give a total error estimate for the derived SST in their Figure 8, which shows a deviation of up to 0.5 ° C in our study region. A main source of uncertainty in the OISST v2 product is the simulation of SST in the presence of sea ice, which might lead to a negative bias when ice concentration are higher than 75% and positive bias for concentrations between 50%

and 75%. See supporting information and Figure S1 for more details and discussion. We then calculated daily mean temperature (T) and density (ρ; using average salinity from the mooring sensors) of the upper 200-m water column. Heat content (Q) per cubic meter of the upper 200 m was then calculated as follows:

$$Q = \rho \cdot V \cdot C_p \cdot T \tag{1}$$

with $V = 200\ \mathrm{m}^3$ for the entire volume and C_p = specific heat of seawater. We used temperatures in degrees Celsius, which is equivalent to using a reference temperature of 0 °C. Heat content change dQ is calculated according to

$$\mathrm{d}Q = \Delta Q/\Delta t \tag{2}$$

with t = time step.

2.4. Vertical Mixing Inferred From Internal Wave-Based Parameterization

During autumn and early winter, when the 800-m mooring at 31°E was frequently blown down due to strong currents and thus *profiled* the water column, the two uppermost CTDs provided temperature and salinity data from a depth range of 20 to 60 m. Combining the hydrographic data with ADCP current shear variance in an internal-wave-based parameterization yields estimates of vertical mixing (Henyey-Wright-Flatte scaling [Henyey et al., 1986], using the same scaling and reference values as in Wijesekera et al., 1993). Dissipation of turbulent kinetic energy, ε at time t, can be estimated as

$$\varepsilon(t) = \frac{1.67}{\pi}(bN_0)^{-2} f \cosh^{-1}\left(\frac{N}{f}\right) j_*^2 E_{\mathrm{meas}}(t)^2, \tag{3}$$

where scaling depth $b = 1,300$ m, reference buoyancy frequency $N_0 = 3$ cph, and vertical mode scale number $j_* = 3$. E_{meas} is estimated as $(\Phi_{uu} + \Phi_{yy})/2$, where $\Phi_{uu,yy}$ are power density spectra of 20-day records of horizontal velocity (u, v) at individual depths, integrated between f (Coriolis frequency) and 1 cph. The CTD data are differenced over 8-m intervals to provide values for N^2.

Vertical diffusivity, K, can then be found using

$$K = \Gamma\varepsilon/N^2 \tag{4}$$

(Osborn, 1980), applying the canonical factor $\Gamma = 0.2$. Combining this with observed vertical temperature gradients, the vertical heat flux, F_H, can be calculated as

$$F_H = -\rho_0 C_p K \mathrm{d}T/\mathrm{d}z, \tag{5}$$

where $\rho_0 = 1,027\ \mathrm{kg\ m^{-3}}$ is the density of seawater and C_p is the specific heat of seawater.

The above calculations will capture not only effects of internal waves but also of wind-driven shear in the upper ocean. It should also be noted that density gradients can be weak in autumn resulting in large uncertainty for diffusivity and heat flux values (see equation (4)). A previous analysis based on the same method to calculate dissipation and diffusivity using a subset of this data set applied the results to estimate the vertical redistribution of nutrients to assess the development of the in situ nitrate pool (Randelhoff et al., 2015). Their results support the levels of diffusivities presented here.

2.5. Ekman Pumping and Associated Upwelling

Surface wind stress for the study region was calculated with

$$\boldsymbol{\tau} = (\tau_x, \tau_y) = \rho_a C_d U_{10} \mathbf{U}_{10} \tag{6}$$

with air density $\rho_a = 1.25\ \mathrm{kg/m^3}$, zonal wind speed U_{10} and wind vector $\mathbf{U}_{10}$ at 10 m above sea level, and using the lower threshold value for the mean air-ocean and air-ice drag coefficient $C_d = 2.7 \cdot 10^{-3}$ for outer marginal ice zones (50% ice concentration; Guest et al., 1995; Lind & Ingvaldsen, 2012). With this approach, we assume that all the momentum in the ice is transferred to the ocean. Daily values of Ekman pumping were calculated using

$$w_e = \frac{1}{\rho_w f}\left(\frac{\partial \tau_y}{\partial x} - \frac{\partial \tau_x}{\partial y}\right), \tag{7}$$

where ρ_w is the mean ocean mixed layer density (taken as 1,025 kg/m^3) and $f = 2\Omega \sin\varphi$ is the Coriolis acceleration at latitude φ; τ_x and τ_y were set to 0 on land. For time series of Ekman pumping at the mooring locations, gridded Ekman pumping was bilinearly interpolated onto the mooring positions.

3. Results

3.1. Hydrographic Variability of the Boundary Current Over the Continental Slope North of Svalbard and Its Impact on the Sea Ice Cover

Both the hydrography and sea ice cover vary considerably during the course of the 1-year deployment period (Figure 2). The mooring sites at 200 and 800 m are ice free in summer and autumn 2012 (Figure 2 b). In November, a patch of sea ice is advected from the north as can be seen from satellite observations (not shown; Tschudi et al., 2016, accessed 29 May 2018) but disappears again completely at the end of the month. The ice only returns in late January, but the sea ice concentration decreases again in the second half of February, after which the ice cover remains dense until complete melt in July. The presence and persistence of sea ice is strongly reflected in the SST (Figure 2c). After high temperatures in autumn 2012, SST was temporarily reduced when sea ice drifted into the study region in mid-November. Following this, the SST increased again, which contributed to ice melt despite air temperatures remaining low (<−9 °C; Figure 2b). The temporary decrease in ice concentration in February occurs concurrently with elevated SST. During periods of dense ice cover (March–June), temperatures in the upper ocean (0–50 m) are markedly reduced. Low temperatures remained in the subsurface layer even after surface temperatures increased due to heating by solar radiation in late June.

In autumn, the core of the AW boundary current is situated close to the 800-m isobath (see Figures 3 and 7 in Pérez-Hernández et al., 2017; Våge et al., 2016, respectively). The variability captured by the 800-m mooring should therefore be representative of the variability in the main part of the boundary current during autumn. Information about potential shoaling or deepening of the boundary current during other seasons is lacking, and the mooring time series might be less representative of the boundary current core outside autumn. In the time series from the 800-m mooring, the AW core with the highest temperatures and highest salinities is generally located between 100- and 500-m depth (Figure 2c; for time series of salinity, see Figure S1b). There is significant variability in both the vertical extent of the AW layer as well as its temperature and salinity throughout the year. The warmest and most saline water is observed in autumn and early winter (September–January), when $T > 3$ °C and $S > 35$, during which time the vertical extent of the AW layer is largest. Both T and S decrease during late winter and remain low during spring and early summer. A similar situation can be seen at the 200-m mooring on the shelf (Figures S1 and S2) with warm and saline water in autumn and early winter, and the onset of cooling at the surface with progression down into the water column in late winter to spring.

The circulation in the study area is generally dominated by the along-slope flow of AW (Figures 2e and 2f). The currents are strongest in autumn and weaker in spring and early summer. A marked event occurred in late November/early December, with currents strong enough to blow down the 800-m mooring as visible from the pressure records in Figure 2d. These enhanced currents in the AW layer led to an increased presence of warm, saline water, which was followed by the disappearance of the sea ice that had been previously advected into the region, and an increase in SST. The current meter time series at 402 and 754 m (not shown) confirm that velocities are elevated throughout the water column. This is concurrent with higher temperatures and salinities also at depth, suggesting an increase in the vertical extent of the AW layer at the 800-m mooring. The velocities at 402-m generally follow the same pattern of variability as recorded by the shallower ADCPs. The lowest current meter, situated roughly 100 m above the sea floor, shows the same pulses of strong currents during autumn and winter but higher velocities from March onward during the ice-covered period. The stronger velocities in late November/early December are also recorded on the shelf, albeit to a lesser degree (Figure S2). The 200-m mooring also shows similar elevated temperatures and salinities along with a temporary decrease in density in November/December.

Various processes such as heat exchange with the atmosphere and wind- or tide-induced mixing can influence the upper ocean heat content north of Svalbard. In the following sections, we begin by investigating heat content changes of the water as it progresses from the upstream mooring at 22°E to the main mooring line at 31°E (for temperature recorded at the upstream mooring, see Figure S3). While advection is likely the largest contributor to the local heat content variability, local processes can lead to significant vertical fluxes which influence the heat budget. After an initial look into heat exchange at the ocean-atmosphere interface, we investigate the role of vertical fluxes in the water column as deduced from current shear variance as well as the influence of tides. While wind-driven upwelling is a well-documented process in parts of the Canadian Arctic (e.g., Pickart et al., 2013), the shelf geometry north of Svalbard is not favorable for shelf break upwelling driven by along-slope winds (Randelhoff & Sundfjord, 2018). We show, however, that Ekman pumping can lead to

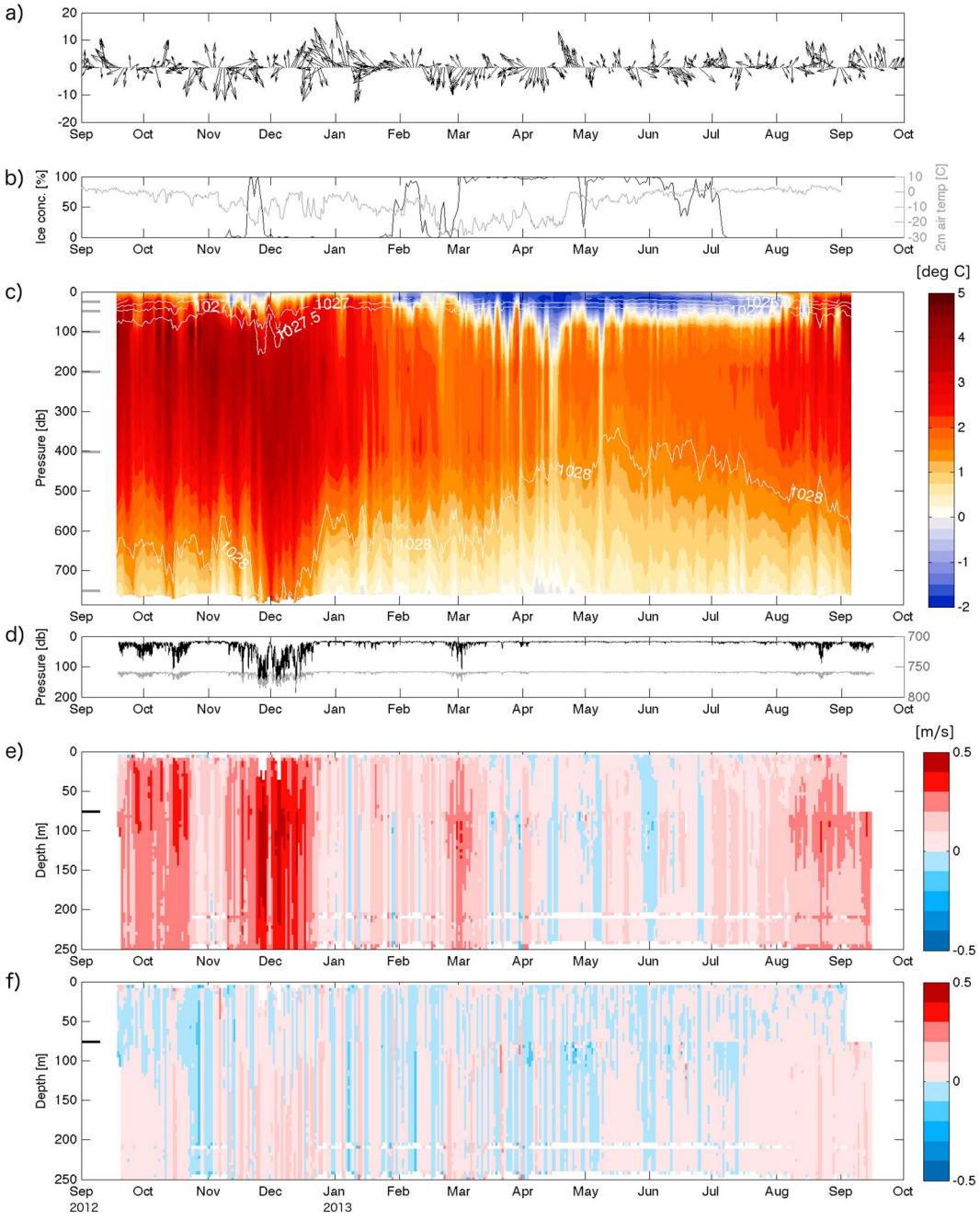

Figure 2. Time series at the 800-m mooring site. (a) Daily wind vectors at 10 m above sea level. (b) Sea ice concentrations and 2-m air temperature. (c) Daily averaged potential temperature from sea surface temperature and CTD sensors on the mooring. The white contour lines show density. Gray markers on the left *y* axis indicate average sensor depth. (d) Daily pressure from top (black, left-hand *y* axis) and bottom (gray, right-hand *y* axis) CTD sensors. (e) Daily averaged along-slope current from the combined acoustic ADCP record. The black marker on the *y* axis shows where the ADCP records were joined. (f) Same as (e) except for the across-slope current.

instances with considerable isopycnal uplift. To fill in the 3-D picture of processes affecting the heat content at our main mooring site, we also discuss the potential role of eddies for cross-slope redistribution of heat.

3.2. Heat Content and Along-Slope Heat Loss in the Boundary Current

Heat content in the upper 200 m, that is, from the core of the AW layer to the surface, experiences a seasonal cycle with highest values in autumn and a minimum in spring (Figure 3a). As expected, heat content is higher at 22°E than at 31°E as heat is lost during the eastward transit. Over the entire deployment period, the upper

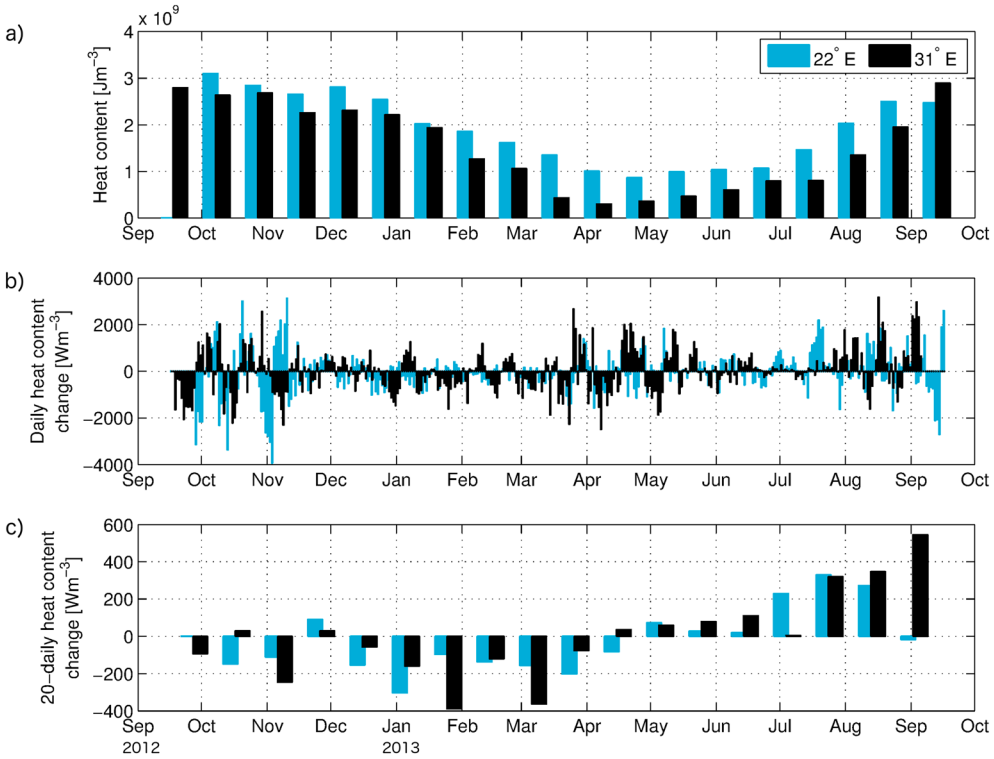

Figure 3. (a) Twenty-day average of heat content in the upper 200-m water column at both 800-m moorings relative to 0 °C. (b) Seven-day running average of daily heat content change for the upper 200 m at the 800-m moorings at 22° and 31°E. (c) Twenty-day average heat content change.

ocean heat content difference between the two moorings is $4.8 \cdot 10^8$ J/m^3, which amounts to a heat loss of 16.7 W m^{-2} over the 145-km distance. Figures 3b and 3c show heat content change in the upper 200 m at the upstream and the main 800-m mooring on short (daily) and longer (20-day averaged) temporal scales, respectively. While there is considerable variability throughout the mooring record, changes are largest during autumn and spring, whereas the late winter period and especially the summer period are more stable. The seasonal cycle during our study period is similar at both locations; however, some differences exist. Changes in heat content at the western mooring often show up after a delay of several days to weeks at the eastern mooring, demonstrating the importance of advection in the region. Nevertheless, changes occur at 31°E that are not recorded at the western mooring first (and vice versa), indicating the importance of local processes for redistribution of heat. Covariance analysis using lagged correlations confirms that over 80% of the variability in the 20-day heat content change at 31°E is driven by changes upstream, whereas changes on daily to weekly time scales are dominated by local processes.

The travel time between the moorings at 22°E and 31°E can be assessed through the correlation between the (daily averaged) 50-m temperature records at the upstream mooring and the main 800-m mooring. For the entire time series the maximum correlation (0.78) corresponds to a 5-day time lag between the two sites. A similar lag is found for all seasons. Correlation analyses for shorter periods (order 100 days) give lower values than the whole time series, which indicates that the seasonal signal in temperature might increase the full-length correlation value. For late winter, when the temperature signals are weaker and upper-column stratification reduced, the time lag found through correlation analysis might also reflect bias from surface processes occurring more or less simultaneously at both locations. We thus expect that the true travel time is longer when the currents are weaker in spring and summer.

The ADCP data from 31°E yield a deployment mean along-slope current speed of 0.12 m/s at 50-m depth with strong seasonality: In the autumn (until 21 December) the mean speed is 0.24 m/s compared to 0.09 m/s for the remaining period. The mean travel time based on these values thus varies between 1 week in autumn to nearly 3 weeks in spring. We therefore choose a 2-week lag to calculate the difference in weekly mean temperatures at the two moorings as shown in Figure 4c. The temperature at 50-m depth between the

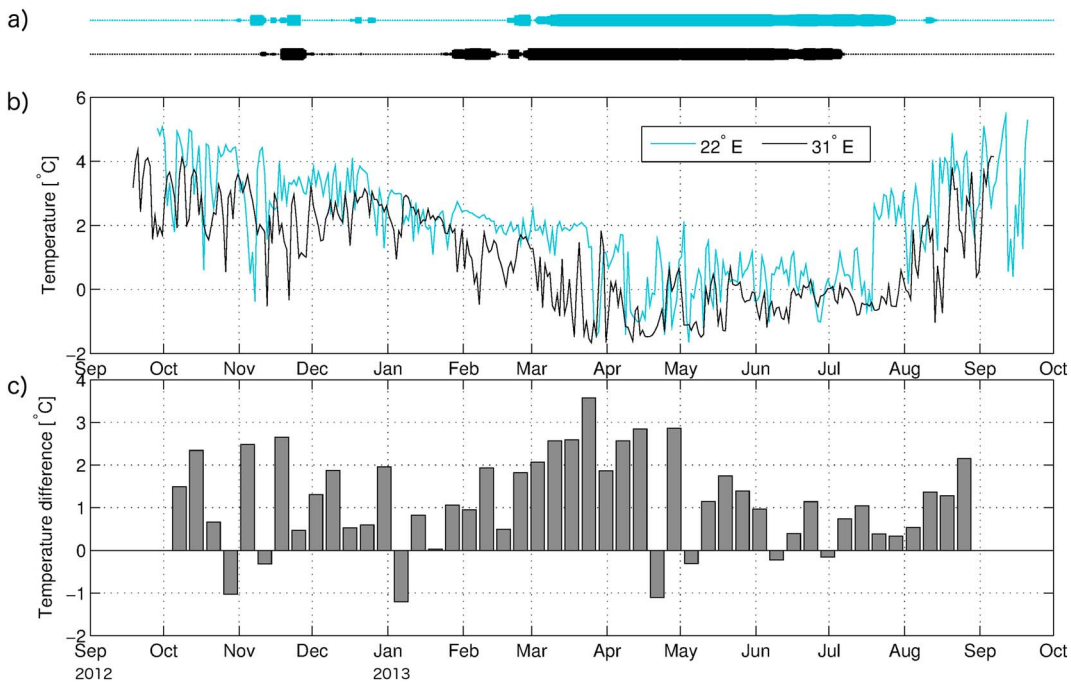

Figure 4. (a) Ice coverage at 22 (blue) and 31°E (black). The thickness of the bars indicates ice concentration between 0 (thinnest) and 100% (thickest). (b) Daily averaged temperature at 50 m at 22° and 31°E. (c) Difference (22°E to 31°E) of weekly means with a 2-week lag to account for the passage of the 145-km distance between the moorings.

upstream 800-m mooring at 22°E and the 800-m mooring in the main array at 31°E is shown in Figure 4 b. The upstream water is considerably warmer most of the time, typically by as much as 1–2 °C (see also Figure S3).

The strong event with increased currents in late November/early December recorded at the main 800-m mooring does not show up clearly in the daily heat content changes (Figure 3b). However, the 20-day averages display a jump from negative to positive heat content change, that is, a heat gain in the upper ocean (Figure 3c). This difference between the daily and the 20-day averages indicates the different time scales involved regarding advective or local signals (Figure 3a), which possibly are caused by local differences in ice coverage leading to both direct and indirect effects (e.g., limiting direct air-sea heat exchange and/or changing surface stratification and thus mixing and vertical fluxes). As cooling from the surface sets in later in winter, combined with reduced temperatures and salinities in lower layers, the heat content is steadily lowered from January until late March, when the upper ocean starts gaining heat again. Shortly after this, in late April, an opening in the ice pack occurs followed by strong short-term heat loss. From the end of July, heat content changes are mostly positive and the upper ocean heat content increases throughout the summer into autumn.

Assuming uniform heat loss at 50-m depth along the 800-m isobath in the study area, the magnitude of the loss can be estimated from the temperature difference between the two mooring sites as shown in Figure 4c. Again, seasonality is strong. We estimate mean values of 36 W m^{-2} for autumn and early winter (September–March) and 15 W m^{-2} for spring and summer (April–September). Two-month-long periods in October–November and February–March have mean heat loss estimates >50 W m^{-2}. These values, which are associated with periods of elevated heat loss, are significantly higher than the estimate based on the 0- to 200-m heat content difference between the two moorings. This suggests that losses are enhanced near the surface, whereas the AW layer retains most of its heat.

3.3. Vertical Heat Flux at 31°E

3.3.1. Air-Sea Heat Fluxes

Heat fluxes at the air-sea interface vary with season and are influenced by the presence of sea ice. Incoming shortwave radiation is only available from mid-March to mid-September when the sun rises above the horizon. Temperature gradients between the ocean and the atmosphere are largest during winter, leading to high

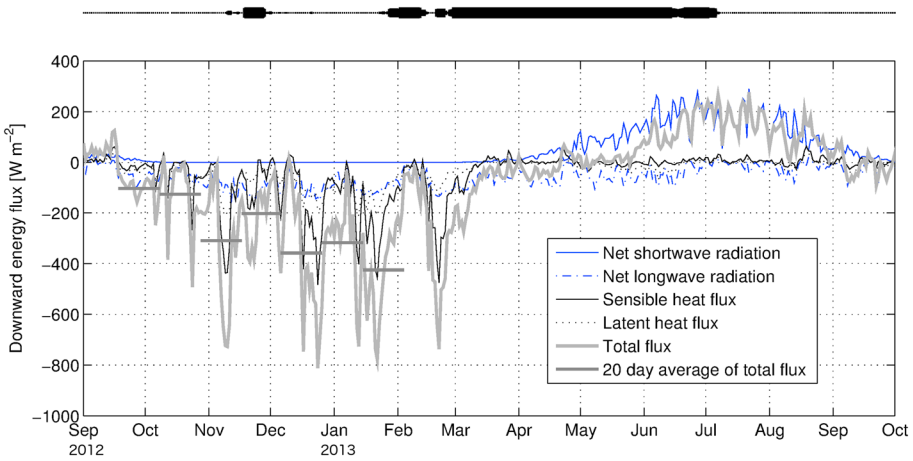

Figure 5. Energy budget at the ocean-atmosphere interface from ERA-Interim data (Dee et al., 2011) at the main 800-m mooring location. Positive = downward flux (i.e., from atmosphere to ocean), negative = upward flux. Total flux is the sum of shortwave and longwave radiation and sensible and latent heat flux. The bar at the top indicates presence of sea ice at the main 800-m mooring; see also Figure 4.

oceanic sensible heat loss in the absence of consolidated sea ice. The arrival of sea ice strongly decreases sensible and latent heat loss and hence reduces the heat flux variability in late winter and spring (Figure 5).

During September to March, the ocean loses on average over 200 W m^{-2} heat to the atmosphere, whereas in March to August, it gains around 80 W m^{-2} (Figure 5). Several notable heat flux events occur during autumn and winter, when over periods of 5 days to 2 weeks, heat loss exceeds 400 W m^{-2}. Intermittent periods with weak heat fluxes are connected to the presence of sea ice inhibiting exchange between the ocean and the atmosphere, which is most pronounced in the first half of February (Figures 2b and 5). For a 1-week period (4–10 February), ice concentrations are high following a period with easterly to southerly winds and air temperatures of −5 to −15 ° C (Figures 2a and 2b). During that time, the average oceanic heat loss to the atmosphere is about 58 W m^{-2}. The 3-week period that follows is characterized by predominantly northerly winds that disperse the ice pack and advect cold air masses, lowering air temperatures to nearly −30 ° C. The large temperature gradient between the air and the open water lead to an average ocean heat loss of 331 W m^{-2} during 11 February to 1 March. Between March and July, the region remained ice covered with strongly reduced air-sea fluxes of ∼9 W m^{-2}. The variability observed in the air-sea heat flux is not directly reflected in the ocean heat content at the 800-m mooring (Figure 3).

3.3.2. Vertical Heat Flux Estimate From Shear Variance and Hydrography

Dissipation in the upper water column (from current shear and stratification profiles, see section 2.4) is periodically enhanced (>10^{-8} W/kg) in autumn and early winter. Highest values are typically found above 30 m (Figure 6, left panel) and correspond to strong wind events (Figure 2a). Lower dissipation coincides with high sea ice concentrations (e.g., November to early December), when sea ice possibly reduces the transfer of wind energy and introduces a melt water layer, restricting the depth range of wind-driven mixing. In late January, sea ice concentrations were low, but potential ice melt could introduce melt water, which increases the stability in the surface layer above our measurements. Nevertheless, dissipation in the 20- to 30-m interval is enhanced compared with dissipation in deeper layers and is larger than during the late November period of high ice concentrations.

Heat fluxes exceeding 100 W m^{-2} are seen in the 20- to 30-m interval, while the heat flux is typically around 20–50 W m^{-2} at 50-m depth (Figure 6, right panel). These estimates compare well with the independent calculations of along-slope heat loss over the 800-m isobath for autumn 2012, where 20-day means at 50-m depth were around 30 W m^{-2} (see section 3.2). The periods of strong heat flux correspond with the periods of strong dissipation, with the exception of late September to early October when mixing was moderately enhanced but the heat flux did not exceed 50 W m^{-2}. During this time the stratification was strong and the temperature gradient modest in the 20- to 30-m depth range.

Air-sea fluxes averaged over the same periods as dissipation and upper ocean vertical heat flux vary in similar fashion, particularly in the absence of sea ice (Figure 5). In general, air-sea fluxes are higher than the

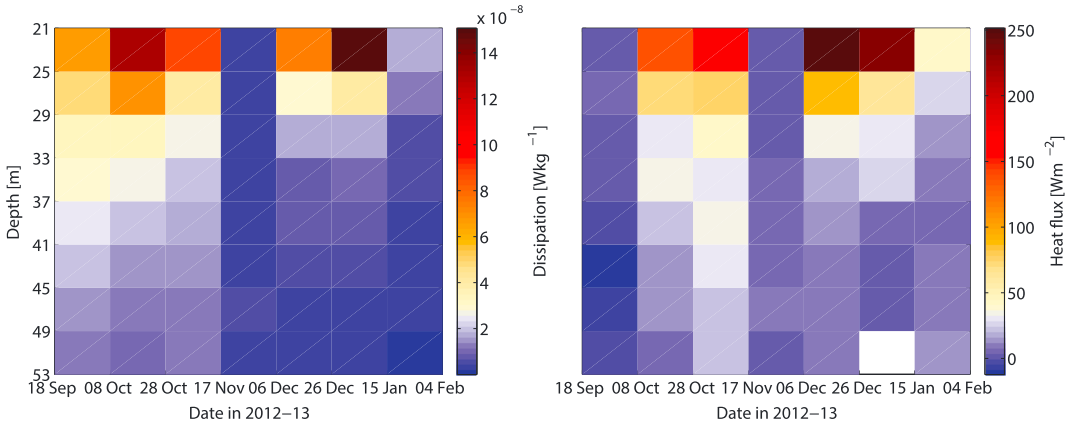

Figure 6. Twenty-day averages of turbulent kinetic energy dissipation (left panel) and vertical heat flux (right) from ADCP current shear variance, stratification, and temperature gradient from the upper part of water column for the autumn-early winter period when the 800-m mooring was being blown down frequently. The white field in the lower layer in late December-early January is due to lack of CTD data in that period.

subsurface heat flux. This is to be expected as long as there is a temperature gradient in the water column, since wind-induced vertical mixing typically decreases from the uppermost part of the water column to the 20- to 30-m depth interval and below. If near-surface lateral heat resupply is not sufficient to maintain the heat content, excessive surface heat loss will cool the upper part of the water column over time. During 17 November to 6 December, the period with a strong wind event and an average sea ice concentration of 35%, heat loss to the atmosphere is lower than in the ice-free periods before and after. The subsurface vertical mixing and heat flux are also reduced during this period, possibly the result of strengthened stratification due to freshening of the near-surface layer. The largest difference between surface and water column fluxes occurs in late January (15 January to 4 February). Then, air-sea heat loss reaches its maximum, while heat flux in the upper ocean is significantly reduced. During this period, the ice cover is building up again, but average concentrations are still quite low (16%). Air temperatures are comparable to the autumn period with reduced upper ocean vertical heat flux, and both periods have average winds in excess of 5 m/s. The major differences lie in the ocean: Freshwater is introduced from melting sea ice, hampering vertical mixing, and temperature in the subsurface layer has started to decrease (Figure 2c). Thus, less heat is available and the temperature gradient in the upper several tens of meters is reduced, potentially as a result of the continuously large air-sea heat loss. During the ensuing weeks, air-sea fluxes are also strongly reduced, until more upper-ocean heat becomes available again in late February (Figure 2).

3.3.3. Effect of Tides on Mixing

Tides are comparatively weak over the deep Arctic Basins but can be considerable in certain continental slope and shelf regions of the Barents, Kara, and Laptev Seas (Padman & Erofeeva, 2003). Tides are known to interact with irregular topography along the slopes and shelves to promote vertical mixing through breaking internal tides and shear instabilities (Rippeth et al., 2015). Near the M_2-critical latitude (~75°N), tides were shown to be strongly dependent on stratification and lead to shear instabilities and enhanced turbulent dissipation (Janout & Lenn, 2014; Lenn et al., 2011). Considering the importance of turbulence and dissipation for vertical fluxes, we next investigate the dominant frequencies that control the dynamics above the north Svalbard continental slope by performing a rotary spectral analysis (Gonella, 1972) on the vertical shear records at both the 200- and 800-m mooring locations. Shear as well as current (not shown) spectra at both locations are dominated by clockwise rotating semidiurnal frequencies, in particular the M_2 tide (Figure 7). The spectra underline that tides are much more energetic at the shelf break (200-m mooring) compared with the deeper slope. The record also resolves several M_2 overtides (M_4, M_6, and M_8) in both currents (not shown) and shear spectra (Figure 7), which points to nonlinear interaction of the M_2 tide with the bottom topography at the 200-m mooring location with potential relevance for mixing as well. This is further underlined in an amplification of the counterclockwise component, which is not the case at the deeper location.

Harmonic analysis using the Matlab T_Tide package (Pawlowicz et al., 2002) was performed on the current records to extract the relevant tidal constituents, with focus on the dominant M_2 constituent and their

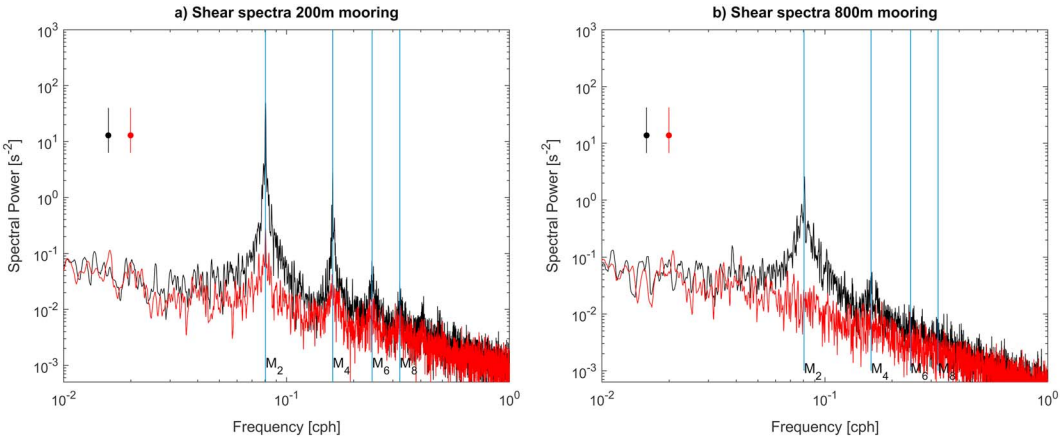

Figure 7. (a) Clockwise (black) and counterclockwise (red) rotating component from rotary spectra analyses (Gonella, 1972) of vertical shear (i.e., the vertical difference in current velocity between 20 and 100 m. The analyses were performed on the 200-m (left) and 800-m (right) mooring ADCP records. The inset vertical lines indicate the confidence interval. The frequency of the M_2 tide and its overtides (M_4, M_6, and M_8) are indicated by the thin blue vertical lines.

parameters. In order to assess the seasonal variability of the tidal structure, we performed 30-day overlapping tidal analyses for the 200-m mooring's current record in the upper 100 m (Figure 8). The M_2 tides appear to be impacted by the sea ice cover as well as by stratification. While the tides are more homogeneous during early winter when sea ice was still absent, a subsurface maximum at 60 m occurs as soon as the region is ice-covered (February – August). This subsurface tidal maximum generally coincides with the presumed depth of the pycnocline (Janout & Lenn, 2014). While CTD records from above 100 m are unfortunately not available from the 200-m mooring (Table 1), the seasonal progression of the top 100-m hydrography can be derived from the 800-m mooring record. As previously described, the temperatures at 100 m are relatively stable (2 – 4 ° C) compared to 20 and 40 m (between near freezing to >4 °C). After reaching a maximum in late autumn, coincident with the strong along-slope flow (Figure 2), temperatures are relatively homogeneous in the upper 100 m until February and also in a period where the tidal structure is largely homogeneous. Beginning in February 2013, sea ice is present and the temperatures at 20 m become highly variable due to mixing and cooling and finally arrives at the freezing point, which implies that a winter pycnocline is established somewhere between 20 and 100 m. This pycnocline persists until August 2013, after the sea ice disappeared.

Acoustically profiled currents and the tidal structure can provide useful information regarding stratification in ice-covered regions in the absence of upper layer instruments (Janout et al., 2016). Considering that stratification generally suppresses turbulence and hence vertical mixing, enhanced tidal shear at the pycnocline thus presents a mechanism to counteract this suppression and contribute to diapycnal mixing between the 2 °C warm water at 100 m and the near-freezing surface waters. The considerable semidiurnal tidal currents and shear are especially relevant at the shelf break and are likely a source of energy and dissipation and hence important for vertical mixing there, as supported by observations (Rippeth et al., 2015) and models (Luneva et al., 2015). Moored (ice track-capable ADCP) ice drift measurements generally show semidiurnal oscillations in a mobile ice cover in other regions where tides are important (Janout & Lenn, 2014). The decreasing role of tides manifested in the shear spectra between our 200- and 800-m moorings (Figure 7) implies that surface currents and hence the ice cover above the continental slope diverges twice daily. The likely consequence is enhanced lead openings and increased air-sea fluxes, which underlines the need for further studies on the effect of tides for the regional heat budget.

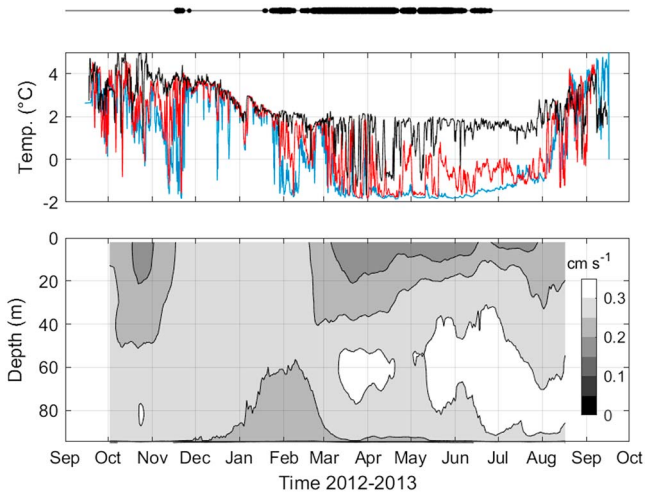

Figure 8. (top) Sea ice concentration (as in Figure 4, middle) temperature at 20 m (blue), 40 m (red), and 100 m (black, bottom) major axis of the M_2 (cm/s) throughout the year-long deployment.

3.4. Wind-Driven Vertical Transports

Several studies have demonstrated the importance of vertical fluxes associated with wind-driven shelf break upwelling in the Canadian Basin of the

Arctic Ocean (e.g., Carmack & Chapman, 2003; Pickart et al., 2009; Schulze & Pickart, 2012). The shelf north of Svalbard is 150–200 m deep versus 50–60 m in the Beaufort Sea where upwelling is particularly common. The much greater depth north of Svalbard implies that shelf break upwelling is not likely to be important here; the outer shelf is too deep for the surface and Ekman layers to overlap and interact (see Randelhoff & Sundfjord, 2018). In addition, the wind field is highly variable both in strength and direction with only few short periods of easterly (i.e., upwelling favorable) winds lasting several consecutive days (Figure 2a). Using the same approach as Lin et al. (2018) applied to detect upwelling events in the Beaufort Sea, we were not able to identify similar events at our shelf break mooring location (200-m bottom depth) related to the wind forcing (Figure S4). Furthermore, assuming that shelf break upwelling should lead to isopycnal tilting, we compared the density at both 100 and 200 m from our two moorings with density from a mooring concurrently deployed 10 km farther offshore near the 2,100-m isobath (Perez-Hernandez, personal communication). No events of density difference change in response to upwelling favorable winds were detected.

Independent of the coast and shelf geometry, upward and downward Ekman pumping due to divergent or convergent wind stress can contribute to vertical transport of water and thus heat. Figure 9 shows seasonal averages of wind stress and wind stress curl over the broader region for the period September 2012 to August 2013. In general, positive wind stress curl, supporting upward pumping, prevails at the mooring sites. During winter, both Ekman transport and pumping are variable with strong episodes of varying directions (Figures 10a and 10b). The largest negative pumping events take place in autumn and early winter, but positive Ekman pumping dominates. Over the period September 2012 to August 2013, we estimate an overall net upward pumping of on average 8.7 cm/day. After a short period of overall negative pumping in November with a suppression by over 6 m, several strong positive episodes occur in December and January with >200 cm/day vertical movement. The average pumping for 15 December 2012 to 14 January 2013 is 65.1 cm/day, which results in an accumulated uplift of 19.5 m in that period (Figure 10). In March–May, theoretical Ekman pumping is modest with an average 6.5 cm/day. In this period, sea ice concentrations are near 100%, and transfer of wind stress to the ocean and thus Ekman transport is reduced. In the ice-free summer season from mid-July, Ekman pumping is around 4.6 cm/day.

To detect Ekman pumping in the mooring record, we extracted a time series of average wind stress curl at the 200- and 800-m mooring location on the main array and attempted to match events of large wind stress curl (positive or negative) with changes in density. At the 200-m mooring, we used density directly from the CTD sensors situated at 104-, 131-, and 180-m depth. We do not find any clear pattern in the mooring record that could consistently be associated with strong wind events. Only the very large uplifts derived from wind stress curl in late December and early January can be matched with increasing density. At the 800-m mooring, the water column is too weakly stratified for a signal to be detected in either density records from the CTD sensors or the interpolated time series.

3.5. Cross-Slope Redistribution of Heat

Part of the along-slope heat loss will be lateral, including slope-shelf exchange and a portion of the flow turning south into the Kvitøya Trough (Pérez-Hernández et al., 2017). We assume that the major part of the advective loss to the shelf and the trough occurs from the up-slope part of the boundary current and does not affect the heat content over the 800-m mooring. Basinward losses, and in particular shedding of mesoscale eddies, can potentially be a larger sink for the central and outer part of the boundary current. During the 2012 A-TWAIN cruise, warm-core anticyclonic eddies were observed over the deeper part of the slope (Våge et al., 2016). In 2013, a cyclonic eddy was detected (Pérez-Hernández et al., 2017). As boundary current eddies often form in dipole pairs, the cruise-based observations suggest that warm-core eddy shedding occurs at least intermittently in this area. A numerical study, analyzing simulations from an eddy-resolving model (Regional Ocean Modelling System; ROMS, horizontal resolution 800 × 800 m; see Crews et al., 2018) from the slope area north of Svalbard, identifies and tracks numerous eddies forming there. In that study, the area east of 20°E appears to be particularly important with respect to shedding eddies that actually emanates from the boundary current and travel into the deep basin. On average, around one eddy per week leaves the boundary current in that area, but only a few of these will actually cross our main mooring array. Conservative estimates of the volume flux associated with AW eddies amount to around 0.1 Sv for the area from 0° to 45°E; based on the findings in Crews et al. (2018) a rough estimate for our study region is thus 0.03 Sv. Therefore, even though the overall loss of AW from the boundary current for the area studied by Crews et al. (2018) might be significant, the model-based estimates indicate that the local loss in our study region is on the order of 1% of the volume flux of AW in the boundary current (3.0 ± 0.2 Sv; Beszczynska-Möller et al., 2012).

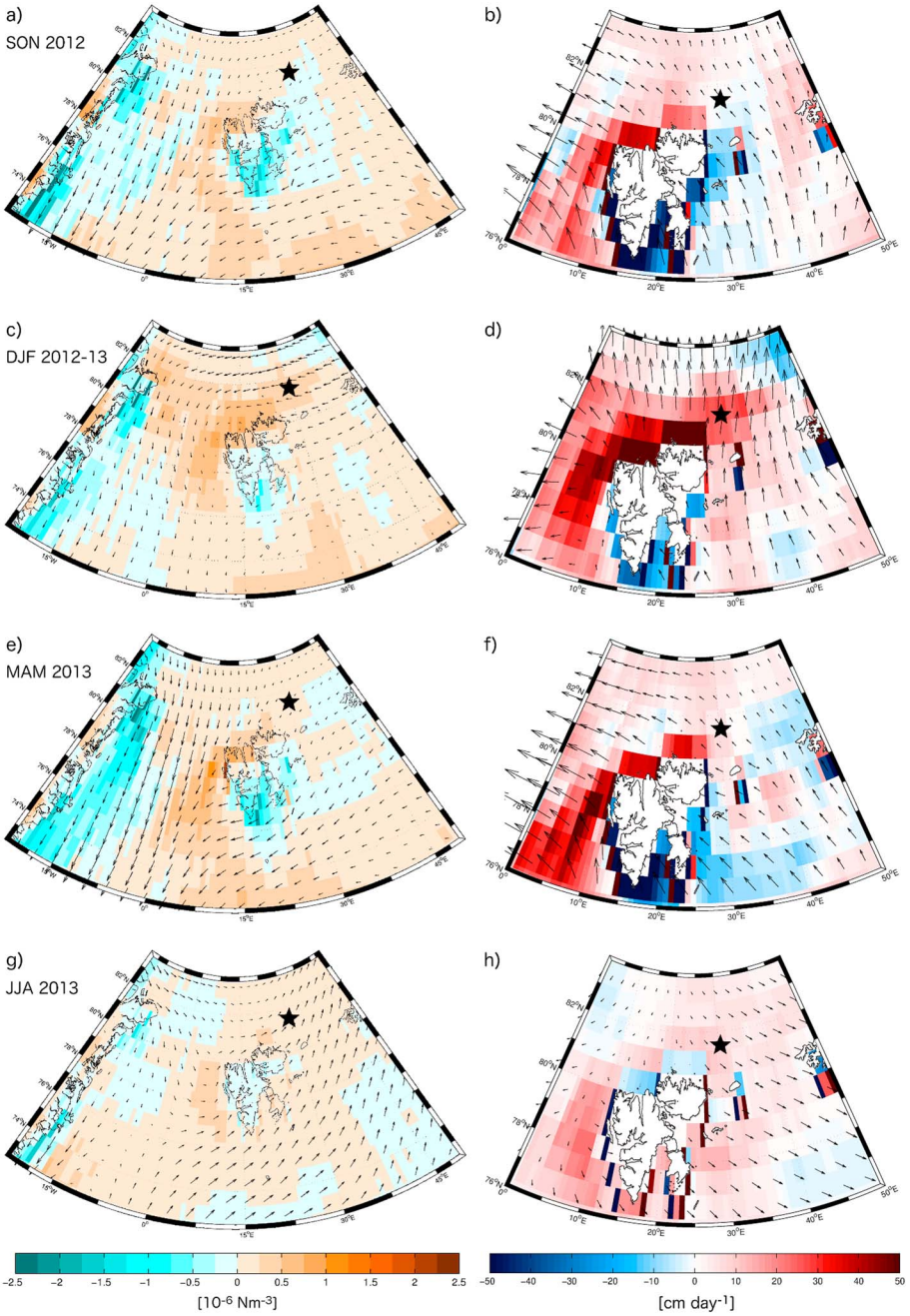

Figure 9. Seasonal averages of wind stress (arrows; every fourth data points along the longitudinal axis) and wind stress curl (background color) on the left, Ekman transport (arrows; every fourth data point along the longitudinal axis) and Ekman pumping (background color; positive values are upward) on the right. (a, b) September–November 2012. (c, d) December 2012 to February 2013. (e, f) March–May 2013. (g, h) June–August 2013. The location of the main mooring line is indicated by the black star.

Eddies can be identified in a mooring time series as concurrent anomalies in temperature or salinity and across-slope velocity. In the records from the 800-m mooring, only one clear example of an anticyclonic (warm-core) eddy was detected as a semiconcurrent drop in temperature and increased up-slope velocity followed by an increase in temperature and down-slope velocity. Examples of current meandering are, however, plentiful. In these cases, strong decreases in temperature are followed by a return to mean values without an ensuing positive temperature anomaly, which would be indicative of warmer water being moved away from the AW core. The lack of eddy signatures in our data suggests that warm-core eddies detach further off-shelf

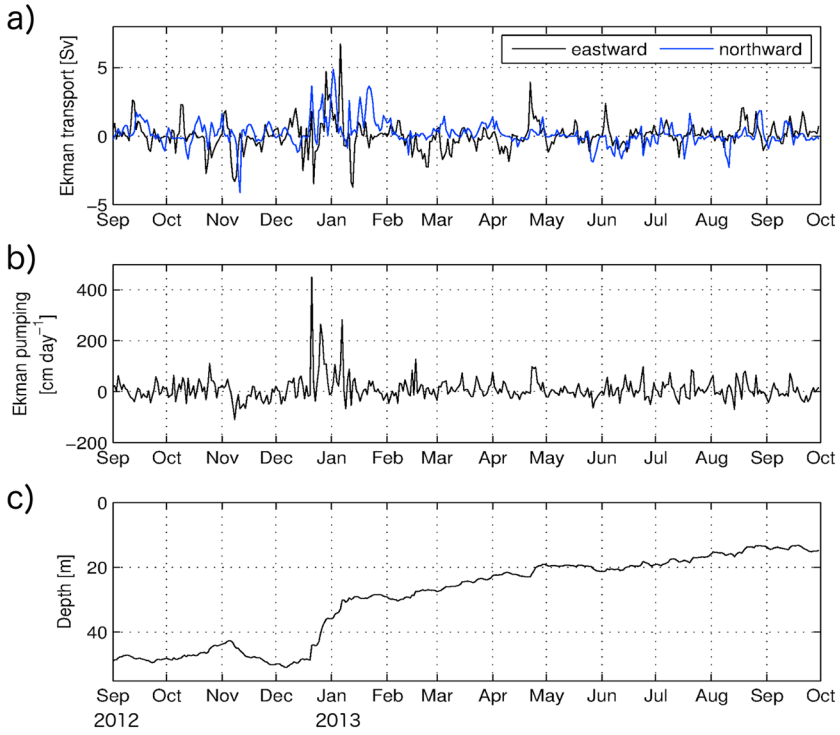

Figure 10. (a) Daily average Ekman transport resulting from local wind stress at the 800-m mooring. (b) Rate of resulting Ekman pumping. (c) Accumulated theoretical lift of a water parcel starting at the bottom of the Ekman layer due to Ekman pumping (assuming a stationary water column). Start depth was chosen as 49 m corresponding to the average depth of one of the CTD sensors on the 800-m mooring.

than our moorings, that is, closer to the maximum gradient between the AW boundary current and the colder and fresher waters over the deeper slope and basin.

4. Discussion and Conclusions

The continental slope region north and northeast of Svalbard is crucial for modification of AW at the beginning of its journey as a boundary current circulating throughout the Arctic Ocean. Figure 11 presents a summary schematic of the relevant processes for the AW heat budget in sea ice-free autumn and winter and ice-covered spring and early summer conditions as presented in section 3 and discussed in this section. From mooring records at 22° and 31°E, we estimate an annual mean heat loss of the upper ocean above the AW core toward the surface of 16.7 W m^{-2} with shorter events having an order of magnitude larger vertical heat fluxes. This heat loss manifests itself as an average temperature difference between the two mooring locations of about 0.8 ° C at 50-m depth and 0.5 ° C for the maximum temperature in the AW core. Cokelet et al. (2008) found higher values from observations conducted in October–November 2001, whereas Pérez-Hernández et al. (2017) did not find a clear decrease in the average AW core temperature in September 2013. This illustrates the large temporal variability in heat loss but also corresponds well with the higher fluxes we find in late fall and winter.

From two different approaches to calculate heat loss during the passage from 22° to 31° E, we find enhancement of heat loss in the near-surface layer above 50 m. In two particular periods, estimates based on 50 m temperatures suggest heat loss of >50 W m^{-2}. In the first case, October–November, this can be related to an increase in negative air-sea heat flux, leading to a cooling of the surface layer as can be expected for autumn. As this seasonal change occurs on large temporal and spatial scales, the signal in the ocean is observable at both moorings. During the second period (February–March) however, the eastern mooring is at first covered by sea ice whereas the upstream mooring is in open water. There, SST is markedly higher. The following ice free period of elevated heat loss at the eastern mooring results in low surface layer temperatures and thus large temperature differences between the moorings. The subsequent high heat loss estimates, however, are at this time forced by local effects, overriding the advective signal.

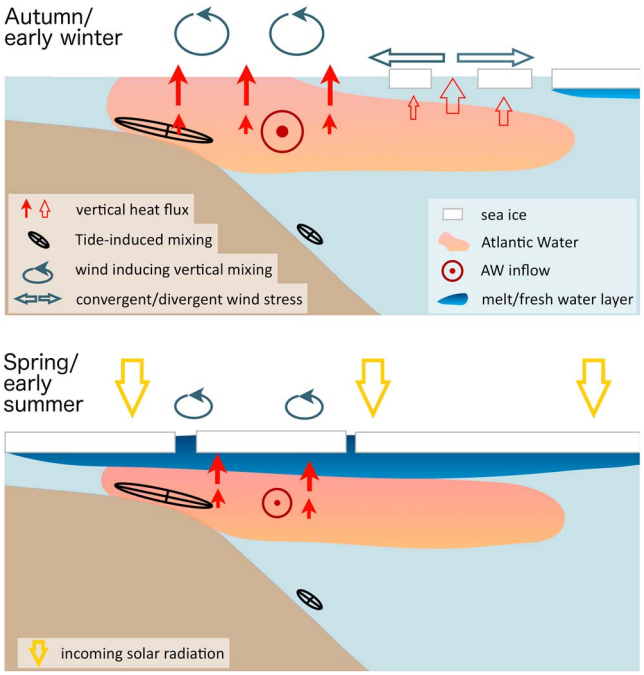

Figure 11. Illustration of the main processes influencing Atlantic Water (AW) heat content during autumn to early winter (top) and spring to early summer (bottom) over the continental shelf and slope north of Svalbard. Vertical heat loss from the AW core upward is mainly driven by wind-induced mixing (gray wind arrows, solid red arrows). Ekman pumping by divergent wind stress (gray open arrows) is a minor source of vertical heat flux (open red arrows). Tide-induced mixing (black tidal ellipses) is significant on the shelf but much smaller in deeper parts. In spring/early summer, a melt water layer under the ice strongly impacts the stratification and hence mixing and vertical heat flux above the AW core. Extensive sea ice cover limits fluxes to the atmosphere and transfer of wind momentum. Solar radiation (yellow open arrows) becomes important toward late spring/early summer.

Vertical fluxes derived from current shear and hydrography for autumn and early winter support the enhancement of heat loss toward the surface. Autumn observations of turbulent fluxes in this area are largely nonexistent. Some distance upstream, Sirevaag and Fer (2009) found values of the same order of magnitude during spring, and episodes with significantly enhanced vertical heat flux were observed during the N-ICE2015 experiment in January–June 2015 (Meyer et al., 2017; Provost et al., 2017), when the drifting ice camp traveled over inflowing AW. These episodes were connected to major storm events and led to significant basal sea ice melt. The agreement between the upper-ocean vertical heat flux estimates and air-sea fluxes during ice-free periods, and the differences connected to the presence of sea ice and changes in wind conditions demonstrate the influence of local environmental conditions.

Tidal analysis of the mooring current measurements shows significant differences between the shelf break/upper slope and the core of the AW current/deeper slope. While we cannot quantify dissipation and heat fluxes based on our data (except for the upper part of the 800-m mooring thanks to mooring blow down in autumn), our findings support earlier measurements of tidally driven upper-slope enhancement of mixing and vertical heat flux in this area (Rippeth et al., 2015). Such tidal mixing has also been inferred farther downstream over the Laptev Sea slope, where tides are weaker but the shelf break shallower (Dmitrenko et al., 2011). Enhanced vertical mixing near the shelf break would, in addition to efficiently bringing heat upward, increase the potential energy over the upper slope relative to the deeper slope. This would tend to set up an off-slope pressure gradient in the upper part of the water column that, when taking rotational effects into account, would serve to enhance the along-slope flow high in the water column relative to the flow over the bottom. The comparatively strong tides and large dissipation in our study area could thus be seen as supporting the observed conversion from predominantly barotropic to more baroclinic flow between Fram Strait and the area north of Svalbard (Pnyushkov et al., 2013). The contrast we find in vertical distribution of tidal velocities between ice-free and ice-covered—stratified and less stratified—periods (Figure 8) indicates that the role of tides for vertical mixing may be reduced with a shift to shorter ice covered periods. On the other hand, less ice and melt water may allow for increased wind-driven vertical heat flux, both in the mixing layer and through internal waves. The downstream effects of longer open water periods north of Svalbard appear to be discernible already (Polyakov et al., 2017), apparently overriding the possible reduction in mixing resulting from lower vertical tidal current shear.

Sea ice acts as a barrier for heat exchange between the atmosphere and the ocean. However, a partial ice cover can actually enhance transfer of wind stress into the ocean as observed by Schulze and Pickart (2012). Martin et al. (2014) confirm this in a model study and suggest that ice concentrations between 80% and 90% are optimal for momentum transfer whereas above 90%, transfer is inhibited. Unfortunately, we do not have dissipation and resulting heat flux estimates for the period in February, when ice concentrations are in that range, and the 50-m temperature differences between 22° and 31° E suggest high heat flux, but we could speculate that the mobile ice cover actually helps to reduce the developing stratification in the surface layer. In periods when the ice cover is extensive over the AW boundary current, we see that the increased stratification due to melt water input in the surface layer suppresses vertical heat flux. In years with larger transport of sea ice to the slope region, that is, a longer ice-covered period, we therefore expect the heat loss from the AW boundary current to be lower compared to years with less sea ice. More of the incoming AW heat can thus be retained for the onward journey. In years with less sea ice, as in several of the recent years, one would expect deeper wind-driven mixing and less pronounced stratification between surface and the AW core, in line with findings from the Laptev Sea slope (Polyakov et al., 2017).

Schulze and Pickart (2012) connect sea ice cover and wind stress to upwelling characteristics in the Alaskan Beaufort Sea. In a numerical study, Carmack and Chapman (2003) showed how the retreat of the sea ice

edge beyond the shelf break enables increased shelf break upwelling under favorable wind conditions in that region. Våge et al. (2016) suggested that the CTD surveys during the deployment cruise for our mooring array show indications of upwelling. However, analyzing the mooring record, we are not able to confirm the occurrence of shelf break upwelling events.

Independent of geographical constraints, wind-induced Ekman pumping has the potential to influence vertical heat fluxes. Yang (2006) showed in an Arctic-wide study how divergent and convergent Ekman transport and associated pumping varied significantly both seasonally and spatially, with highest vertical velocities in autumn and winter in the Beaufort Sea and in Fram Strait. The eastern Fram Strait is dominated by positive pumping, but this is reduced farther to the east at our mooring location. In general though, the southern Nansen Basin and the region north of Svalbard are at least seasonally likely to experience vertical heat flux due to Ekman transport. We find relatively modest but nonnegligible offshore net upward pumping. Following Yang (2006) to calculate upward heat flux associated with this Ekman pumping, we estimate an average heat loss of 3.5 W m^{-2} from 30-m depth. While offshore Ekman pumping does not currently seem to be a major driver of heat exchange north of Svalbard, Ma et al. (2017) report an increase of vertical velocities driven by Ekman transport with eastern Fram Strait being one of the regions with large increases in upward pumping. Lind and Ingvaldsen (2012) found Ekman pumping to be a major driver for AW entering the Barents Sea from the north, and a strengthening of this pumping might contribute to further warming of the Barents Sea.

The very large local autumn and winter heat loss calculated from our in situ measurements along the upper slope north of Svalbard are consistent with the findings of Ivanov et al. (2012) and Onarheim et al. (2014) who argued that winter ice loss north of Svalbard is driven from below by AW inflow. In fact, Figure 3 in Onarheim et al. (2014) shows that the ice loss is largest in the months October to February, the period in which both AW heat content and heat loss in our mooring record is largest.

We presented year-long records from moorings deployed north of Svalbard in the inflow of AW into the Arctic. Our observations document variability in the core of the AW inflow and its heat content. Advection of signals from further upstream accounts for over 80% of the variability in our time series. However, local processes have significant impact on the higher frequency variability. This includes air-sea heat exchange, wind-driven and tidally driven mixing (Figure 11). The high flux values inferred from internal wave parameterization and air-sea reanalysis indicate that the bulk of the heat loss is vertical and not lateral. As seen in autumn 2012, episodes of increased advection and strong wind significantly increase the annual mean heat loss. Sea ice plays a major role by impacting these processes to varying degrees and depending on ice concentrations. A longer time series spanning several years is necessarily to better distinguish seasonal signals and assess changes in the AW inflow and their impact downstream in the Arctic. Our results also demonstrate the need for continuous year-round observations, as significant short-duration episodes of elevated vertical heat fluxes, for example, during storms and in winter, are usually not captured by shipboard surveys, which therefore will not allow for heat content and transport estimates that are representative for longer time periods.

Acknowledgments
We thank the captain and crews of RV Lance, Kristen Fossan, and Ronald Pedersen for the technical support with the mooring deployments and cruises. We are grateful to Vladimir Pavlov for help with data processing and discussions during early stages of the manuscript. The A-TWAIN project is financially supported by the Fram Centre flagship "Sea ice in the Arctic Ocean, technology and agreements." The analysis was partially funded by the Research Council of Norway through the project The Nansen Legacy (RCN 276730). The U.S. component of A-TWAIN was funded by the National Science Foundation under grant ARC-1264098 as well as a grant from the Steven Grossman Family Foundation. The IOPAN contribution to A-TWAIN observations and data analyses were supported by the Polish-Norwegian Research Programme under the project PAVE (Atlantic Water Pathways to the Arctic: Variability and Effects on Climate and Ecosystems, contract POL-NOR/202006/10/2013). The mooring data are available from the Norwegian Polar Data Centre (Sundfjord et al., 2017).

References

Aagaard, K. (1989). A synthesis of the Arctic Ocean circulation. *Rapports et Proces-verbaux des Réunions. Conseil International pour l'Éploration de la Mer*, *188*, 11–22.

Aagaard, K., Foldvik, A., & Hillman, S. R. (1987). The West Spitsbergen current: Disposition and water mass transformation. *Journal of Geophysical Research: Oceans*, *92*(C4), 3778–3784.

Aksenov, Y., Ivanov, V. V., Nurser, A. J. G., Bacon, S., Polyakov, I. V., Coward, A. C., et al. (2011). The Arctic circumpolar boundary current. *Journal of Geophysical Research*, *116*, C09017. https://doi.org/10.1029/2010JC006637

Beszczynska-Möller, A., Fahrbach, E., Schauer, U., & Hansen, E. (2012). Variability in Atlantic water temperature and transport at the entrance to the Arctic Ocean, 1997–2010. *ICES Journal of Marine Science*, *69*(5), 852–863. https://doi.org/10.1093/icesjms/fss056

Carmack, E., & Chapman, D. C. (2003). Wind-driven shelf/basin exchange on an Arctic shelf: The joint roles of ice cover extent and shelf-break bathymetry. *Geophysical Research Letters*, *30*(14), 1778. https://doi.org/10.1029/2003GL017526

Cokelet, E. D., Tervalon, N., & Bellingham, J. G. (2008). Hydrography of the West Spitsbergen Current, Svalbard Branch: Autumn 2001. *Journal of Geophysical Research*, *113*, C01006. https://doi.org/10.1029/2007JC004150

Crews, L., Sundfjord, A., Albretsen, J., & Hattermann, T. (2018). Mesoscale eddy activity and transport in the Atlantic Water inflow region north of Svalbard. *Journal of Geophysical Research: Oceans*, *123*, 201–215. https://doi.org/10.1002/2017JC013198

Dee, D. P., Uppala, S. M., Simmons, A. J., Berrisford, P., Poli, P., Kobayashi, S., et al. (2011). The ERA-Interim reanalysis: Configuration and performance of the data assimilation system. *Quarterly Journal of the Royal Meteorological Society*, *137*, 553–597. https://doi.org/10.1002/qj.828

Dmitrenko, I. A., Ivanov, V. V., Kirillov, S. A., Vinogradova, E. L., Torres-Valdes, S., & Bauch, D. (2011). Properties of the Atlantic derived halocline waters over the Laptev Sea continental margin: Evidence from 2002 to 2009. *Journal of Geophysical Research*, *116*, C10024. https://doi.org/10.1029/2011JC007269

Dmitrenko, I. A., Polyakov, I. V., Kirillov, S. A., Timokhov, L. A., Simmons, H. L., Ivanov, V. V., & Walsh, D. (2006). Seasonal variability of Atlantic water on the continental slope of the Laptev Sea during 2002–2004. *Earth and Planetary Science Letters*, *224*(3-4), 735–743. https://doi.org/10.1016/j.epsl.2006.01.067

Gascard, J. C., Richez, C., & Rouault, C. (1995). New insights on large-scale oceanography in Fram Strait: The West Spitsbergen Current. In W. O. Smith & J. M. Grebmeier (Eds.), *Arctic Oceanography: Marginal Ice Zones and Continental Shelves* (pp. 131–182). Washington DC: American Geophysical Union.

Gonella, J. (1972). A rotary-component method for analysing meteorological and oceanographic vector time series. *Deep-Sea Research*, *19*, 833–846.

Guest, P. S., Glendening, J. W., & Davidson, K. L. (1995). An observational numerical study of wind stress variations within marginal ice zones. *Journal of Geophysical Research*, *100*, 10,887–10,904.

Hattermann, T., Isachsen, P. E., von Appen, W.-J., Albretsen, J., & Sundfjord, A. (2016). Eddy-driven recirculation of Atlantic Water in Fram Strait. *Geophysical Research Letters*, *43*, 3406–3414. https://doi.org/10.1002/2016GL068323

Henyey, F. S., Wright, J., & Flatté, S. M. (1986). Energy and action flow through the internal wave field: An eikonal approach. *Journal of Geophysical Research: Oceans*, *91*(C7), 8487–8495. https://doi.org/10.1029/JC091iC07p08487

Hudson, S. R., Sundfjord, M. A. G. A., Randelhoff, A., Renner, A. H. H., & Divine, D. V. (2013). Energy budget of first-year Aarctic sea ice in advanced stages of melt. *Geophysical Research Letters*, *40*, 2679–2683. https://doi.org/10.1002/grl.50517

Ivanov, V., Alexeev, V., Koldunov, N. Y., Repina, I., Sandø, A. B., Smedsrud, L. H., & Smirnov, A. (2016). Arctic Ocean heat impact on regional ice decay: A suggested positive feedback. *Journal of Physical Oceanography*, *46*, 1437–1456. https://doi.org/10.1175/JPO-D-15-0144.1

Ivanov, V. V., Alexeev, V. A., Repina, I., Koldunov, N. V., & Smirnov, A. (2012). Tracing Atlantic water signature in the Arctic sea ice cover east of Svalbard. *Advances in Meteorology*, *2012*, 201818. https://doi.org/10.1155/2012/201818

Ivanov, V. V., Polyakov, I. V., Dmitrenko, I. A., Hansen, E., Repina, I. A., Kirillov, S. A., et al. (2009). Seasonal variability in Atlantic Water off Spitsbergen. *Deep-Sea Research I*, *56*, 1–14. https://doi.org/10.1016/j.dsr.2008.07.013

Jakobsson, M. E. A. (2012). The Internaltional Bathymetric Chart of the Arctic Ocean (IBCAO) version 3.0. *Geophysical Research Letters*, *39*, L12609. https://doi.org/10.1029/2012GL052219

Janout, M., Hölemann, J., Juhls, B., Krumpen, T., Rabe, B., Bauch, D., et al. (2016). Episodic warming of near-bottom waters under the Arctic sea ice on the central Laptev Sea shelf. *Geophysical Research Letters*, *43*, 264–272. https://doi.org/10.1002/2015GL066565

Janout, M. A., & Lenn, Y.-D. (2014). Semidiurnal tides on the Laptev Sea shelf with implications for shear and vertical mixing. *Journal of Physical Oceanography*, *44*, 202–219. https://doi.org/10.1175/JPO-D-12-0240.1

Koenig, Z., Provost, C., Sennéchael, N., Garric, G., & Gascard, J.-C. (2017). The Yermak Pass Branch: A major pathway for the Atlantic Water north of Svalbard. *Journal of Geophysical Research: Oceans*, *122*, 9332–9349. https://doi.org/10.1002/2017JC013271

Koenig, Z., Provost, C., Villacieros-Robineau, N., Sennéchael, N., & Meyer, A. (2016). Winter ocean-ice interactions under thin sea ice observed by IAOOS platforms during N-ICE2015: Salty surface mixed layer and active basal melt. *Journal of Geophysical Research: Oceans*, *121*, 7898–7916. https://doi.org/10.1002/2016JC012195

Lenn, Y.-D., Rippeth, T. P., Old, C. P., Bacon, S., Polyakov, I., Ivanov, V., & Hölemann, J. (2011). Intermittent intense turbulent mixing under ice in the Laptev Sea continental shelf. *Journal of Physical Oceanography*, *41*, 531–547. https://doi.org/10.1175/2010JPO4425.1

Lenn, Y. D., Wiles, P. J., Torres-Valdes, S., Abrahamsen, E. P., Rippeth, T. P., Simpson, J. H., et al. (2009). Vertical mixing at intermediate depths in the Arctic boundary current. *Geophysical Research Letters*, *36*, L05601. https://doi.org/10.1029/2008GL036792

Lin, P., Pickart, R. S., Moore, G. W. K., Spall, M. A., & Hu, J. (2018). Characteristics and dynamics of wind-driven upwelling in the Alaskan Beaufort Sea based on six years of mooring data. *Deep Sea Research II*. https://doi.org/10.1016/j.dsr2.2018.01.002

Lind, S., & Ingvaldsen, R. B. (2012). Variability and impacts of Atlantic Water entering the Barents Sea from the north. *Deep Sea Research I*, *62*, 70–88. https://doi.org/10.1016/j.dsr.2011.12.007

Luneva, M. V., Aksenov, Y., Harle, J. D., & Holt, J. T. (2015). The effects of tides on the water mass mixing and sea ice in the Arctic Ocean. *Journal of Geophysical Research: Oceans*, *120*, 6669–6699. https://doi.org/10.1002/2014JC010310

Ma, B., Steele, M., & Lee, C. M. (2017). Ekman circulation in the Arctic Ocean: Beyond the Beaufort Gyre. *Journal of Geophysical Research: Oceans*, *122*, 3358–3374. https://doi.org/10.1002/2016JC012624

Martin, T., Steele, M., & Zhang, J. (2014). Seasonality and long-term trend of Arctic Ocean surface stress in a model. *Journal of Geophysical Research: Oceans*, *119*, 1723–1738. https://doi.org/10.1002/2013JC009425

Meyer, A., Fer, I., Sundfjord, A., & Peterson, A. K. (2017). Mixing rates and vertical heat fluxes north of Svalbard from Arctic winter to spring. *Journal of Geophysical Research: Oceans*, *122*, 4569–4586. https://doi.org/10.1002/2016JC012441

Nøst, O. A., & Isachsen, P. E. (2003). The large-scale time-mean ocean circulation in the Nordic Seas and Arctic Ocean estimated from simplified dynamics. *Journal of Marine Research*, *61*, 175–201.

Onarheim, I., Smedsrud, L., Ingvaldsen, R., & Nilsen, F. (2014). Loss of sea ice during winter north of Svalbard. *Tellus A*, *66*, 23933. https://doi.org/10.3402/tellusa.v66.23933

Osborn, T. R. (1980). Estimates of the local rate of vertical diffusion from dissipation measurements. *Journal of Physical Oceanography*, *10*(1), 83–89.

Padman, L., & Erofeeva, S. (2003). A barotropic inverse tidal model for the Arctic Ocean. *Geophysical Research Letters*, *31*, L02303. https://doi.org/10.1029/2003GL019003

Pawlowicz, R., Beardsley, B., & Lentz, S. (2002). Harmonic analysis including error estimates in MATLAB unsing T_TIDE. *Computers and Geosciences*, *28*, 929–937.

Pérez-Hernández, M. D., Pickart, R. S., Pavlov, V., Våge, K., Ingvaldsen, R., Sundfjord, A., et al. (2017). The Atlantic Water boundary current north of Svalbard in late summer. *Journal of Geophysical Research: Oceans*, *122*, 2269–2290. https://doi.org/10.1002/2016JC012486

Peterson, A. K., Fer, I., McPhee, M. G., & Randelhoff, A. (2017). Turbulent heat and momentum fluxes in the upper ocean under Arctic sea ice. *Journal of Geophysical Research: Oceans*, *122*, 1439–1456. https://doi.org/10.1002/2016JC012283

Pickart, R. S., Moore, G. W. K., Torres, D. J., Fratantoni, P. S., Goldsmith, R. A., & Yang, J. (2009). Upwelling on the continental slope of the Alaskan Beaufort Sea: Storms, ice, and oceanographic response. *Journal of Geophysical Research*, *114*, C00A13. https://doi.org/10.1029/2008JC005009

Pickart, R. S., Spall, M. A., & Mathis, J. T. (2013). Dynamics of upwelling in the Alaskan Beaufort Sea and associated shelf-basin fluxes. *Deep-Sea Research I*, *76*, 35–51.

Pnyushkov, A. V., & Polyakov, I. V. (2012). Observations of tidally induced currents over the continental slope of the Laptev Sea, Arctic Ocean. *Journal of Physical Oceanography*, *42*, 78–94. https://doi.org/10.1175/JPO-D-11.064.1

Pnyushkov, A. V., Polyakov, I. V., Ivanov, V. V., Aksenov, Y., Coward, A. C., Janout, M., & Rabe, B. (2015). Structure and variability of the boundary current in the Eurasian Basin of the Arctic Ocean. *Deep-Sea Research I*, *101*, 80–97.

Pnyushkov, A. V., Polyakov, I. V., Ivanov, V. V., & Kikuchi, T. (2013). Structure of the Fram Strait branch of the boundary current in the Eurasian Basin of the Arctic Ocean. *Polar Science*, *7*, 53–71. https://doi.org/10.1016/j.polar.2013.02.001

Polyakov, I. V., Beszczynska, A., Carmack, E. C., Dmitrenko, I. A., Fahrbach, E., Frolov, I. E., et al. (2005). One more step toward a warmer Arctic. *Geophysical Research Letters*, *32*, L17605. https://doi.org/10.1029/2005GL023740

Polyakov, I. V., Pnyushkov, A. V., Alkire, M. B., Ashik, I. M., Baumann, T. M., Carmack, E. C., et al. (2017). Greater role for Atlantic inflows on sea-ice loss in the Eurasian Basin of the Arctic Ocean. *Science*, *356*, 285–291. https://doi.org/10.1126/science.aai8204

Polyakov, I. V., Timokhov, L. A., Alexeev, V. A., Bacon, S., Dmitrenko, I. A., Fortier, L., et al. (2010). Arctic Ocean warming contributes to reduced polar ice cap. *Journal of Physical Oceanography*, *40*, 2743–2756. https://doi.org/10.1175/2010JPO4339.1

Provost, C., Sennéchael, N., Miguet, J., Itkin, P., Rösel, A., Koenig, Z., et al. (2017). Observations of flooding and snow-ice formation in a thinner Arctic sea ice regime during the N-ICE2015 campaign: Influence of basal ice melt and storms. *Journal of Geophysical Research: Oceans*, *122*, 7115–7134. https://doi.org/10.1002/2016JC012011

Randelhoff, A., & Sundfjord, A. (2018). Short commentary on marine productivity at Arctic shelf breaks: Upwelling, advection and vertical mixing. *Ocean Science*, *14*, 293–300. https://doi.org/10.5194/os-14-293-2018

Randelhoff, A., Sundfjord, A., & Reigstad, M. (2015). Seasonal variability and fluxes of nitrate in the surface waters over the arctic shelf slope. *Geophysical Research Letters*, *42*, 3442–3449. https://doi.org/10.1002/2015GL063655

Renner, A. H. H., Hendricks, S., Gerland, S., Beckers, J., Haas, C., & Krumpen, T. (2013). Large-scale ice thickness distribution of first-year sea ice in spring and summer north of Svalbard. *Annals of Glaciology*, *54*(62), 13–18. https://doi.org/10.3189/2013AoG62A146

Reynolds, R. W. (2009). What's new in version 2. OISST webpage. Retrieved from http://www.ncdc.noaa.gov/sites/default/files/attachments/Reynolds2009_oisst_daily_v02r00_version2-features.pdf

Reynolds, R. W., Smith, T. M., Liu, C., Chelton, D. B., Casey, K. S., & Schlax, M. G. (2007). Daily high-resolution-blended analyses for sea surface temperature. *Journal of Climate*, *20*, 5473–5496. https://doi.org/10.1175/JCLI-D-14-00293.1

Rippeth, T. P., Lincoln, B. J., Lenn, Y.-D., Green, J. A. M., Sundfjord, A., & Bacon, S. (2015). Tide-mediated warming of Arctic halocline by Atlantic heat fluxes over rough topography. *Nature Geoscience*, *8*, 191–194. https://doi.org/10.1038/ngeo2350

Rudels, B., Friedrich, H. J., & Quadfasel, D. (1999). The Arctic circumpolar boundary current. *Deep-Sea Research II*, *46*, 1023–1062. https://doi.org/10.1016/S0967-0645(99)00015-6

Rudels, B., Kohonen, M., Schauer, U., Pisarev, S., Rabe, B., & Wisotzki, A. (2014). Circulation and transformation of Atlantic Water in the Eurasian Basin and the contribution of the Fram Strait inflow branch to the Arctic Ocean heat budget. *Progress in Oceanography*, *132*, 128–152. https://doi.org/10.1016/j.pocean.2014.04.003

Schauer, U., Fahrbach, E., Osterhus, S., & Rohardt, G. (2004). Arctic warming through the Fram Strait: Oceanic heat transport from 3 years of measurements. *Journal of Geophysical Research*, *109*, C06026. https://doi.org/10.1029/2003JC001823

Schulze, L. M., & Pickart, R. S. (2012). Seasonal variation of upwelling in the Alaskan Beaufort Sea: Impact of sea ice cover. *Journal of Geophysical Research*, *117*, C06022. https://doi.org/10.1029/2012JC007985

Sirevaag, A., & Fer, I. (2009). Early spring oceanic heat fluxes and mixing observed from drift stations north of Svalbard. *Journal of Physical Oceanography*, *39*, 3049–3069. https://doi.org/10.1175/2009JPO4172.1

Spreen, G., Kaleschke, L., & Heygster, G. (2008). Sea ice remote sensing using AMSR-E 89-GHz channels. *Journal of Geophysical Research*, *113*, C02S03. https://doi.org/10.1029/2005JC003384

Sundfjord, A., Renner, A. H. H., & Beszczynska-Möller, A. (2017). A-TWAIN mooring hydrography and current data Sep 2012–Sep 2013 [Data set]. Norwegian Polar Institute. Retrieved from https://data.npolar.no/dataset/73d0ea3a-fd21-4eab-8eb9-1e033fefcd8e, https://doi.org/10.21334/npolar.2017.73d0ea3a

Tschudi, M., Fowler, C., Maslanik, J., Stewart, J. S., & Meier, W. (2016, accessed 29 May 2018). *Polar Pathfinder Daily 25 km EASE-Grid Sea Ice Motion Vectors, version 3. Subset October 2012–March 2013*. Boulder, CO: National Snow and Ice Data Center. Distributed in netCDF format by the Integrated Climate Data Center (ICDC), University of Hamburg, Hamburg, Germany, https://doi.org./10.5067/O57VAIT2AYYY

Våge, K., Pickart, R. S., Pavlov, V., Lin, P., Torres, D. J., Ingvaldsen, R., et al. (2016). The Atlantic Water boundary current in the Nansen Basin: Transport and mechanisms of lateral exchange. *Journal of Geophysical Research: Oceans*, *121*, 6946–6960. https://doi.org/10.1002/2016JC011715

Vinje, T. (2001). Anomalies and trends of sea-ice extent and atmospheric circulation in the Nordic Seas during the period 1864–1998. *Journal of Climate*, *14*, 255–267.

Wijesekera, H., Padman, L., Dillon, T., Levine, M., Paulson, C., & Pinkel, R. (1993). The application of internal-wave dissipation models to a region of strong mixing. *Journal of Physical Oceanography*, *23*(2), 269–286.

Yang, J. (2006). The seasonal variability of the Arctic Ocean Ekman transport and its role in the mixed layer heat and salt fluxes. *Journal of Climate*, *19*, 5366–5387.